

PAPER

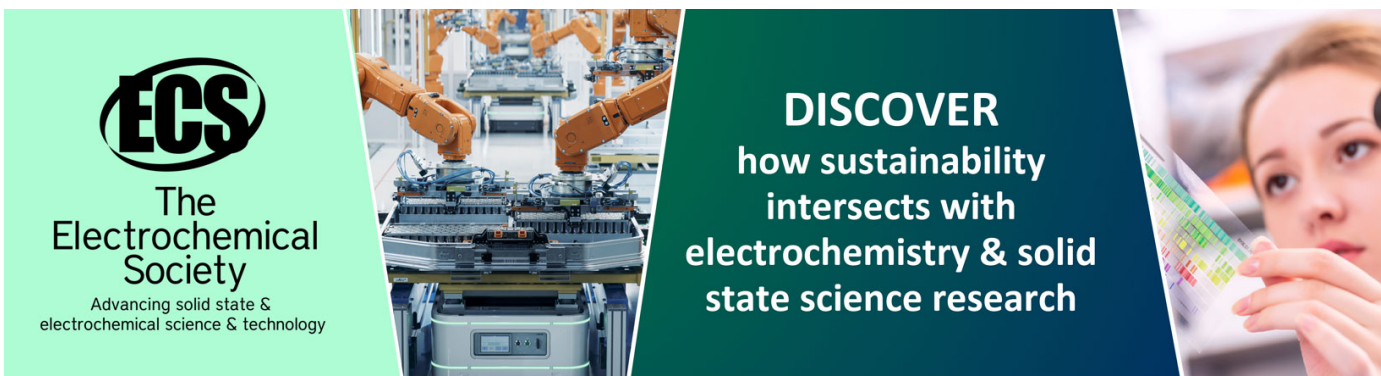
Characterization of 150 μm thick silicon microstrip prototype for the FOOT experiment

To cite this article: Gianluigi Silvestre *et al* 2022 *JINST* 17 P12012

View the [article online](#) for updates and enhancements.

You may also like

- [Assembly and test of prototype scintillator tiles for the plastic scintillator detector of the High Energy Cosmic Radiation Detection \(HERD\) facility](#)
C. Altomare, F. Alemanno, F.C.T. Barbato et al.
- [Silicon Carbide devices for radiation detection and measurements](#)
F La Via, S Tudisco, C Altana et al.
- [A complete MC optical photons tracking simulation of Plastic Scintillator Detectors for the next generation of satellite experiments](#)
C. Altomare, F. Alemanno, F.C.T. Barbato et al.



ECS
The Electrochemical Society
Advancing solid state & electrochemical science & technology

DISCOVER
how sustainability intersects with electrochemistry & solid state science research

Characterization of 150 μm thick silicon microstrip prototype for the FOOT experiment



The FOOT collaboration

Gianluigi Silvestre,^{k,v} Francesca Peverini,^{k,v} Leonello Servoli,^{k,*} Keida Kanxheri,^{k,v} Mattia Barbanera,^k Pisana Placidi,^{k,w} Maria Ionica,^k Mirco Caprai,^k Giovanni Ambrosi,^k Lucia Salvi,^{k,v} Emanuele Fiandrini,^{k,v} Behcet Alpat,^k Andrey Alexandrov,^{j,r,ae,af} Stefano Argirò,^{z,q} Diaz Raul Arteche,^{ab} Nazar Bartosik,^q Giuseppe Battistoni,^h Nicola Belcari,^{b,a} Elettra Bellinzona,^o Silvia Biondi,^{d,s} Maria Giuseppina Bisogni,^{a,b} Graziano Bruni,^d Pietro Carra,^{b,a} Francesca Cavanna,^q Piergiorgio Cerello,^q Esther Ciarrocchi,^{b,a} Alberto Clozza,^g Sofia Colombi,^{o,p} Angelica De Gregorio,^{l,x} Giovanni De Lellis,^{j,r} Alberto Del Guerra,^{b,a} Micol De Simoni,^l Antonia Di Crescenzo,^{j,r} Benedetto Di Ruzza,^o Marco Donetti,^{e,q} Yunsheng Dong,^h Marco Durante,^{f,ad} Riccardo Faccini,^{l,x} Veronica Ferrero,^q Christian Finck,ⁿ Elisa Fiorina,^q Marta Fischetti,^u Marco Francesconi,^{b,a} Matteo Franchini,^{d,s} Gaia Franciosini,^{l,x} Giuliana Galati,^{ag} Luca Galli,^a Valerio Gentile,^{ac} Giuseppe Girauda,^q Ronja Hetzel,^c Enzo Iarocci,^g Aafke Christine Kraan,^a Chiara La Tessa,^{o,p} Martina Laurenza,^g Adele Lauria,^{j,r} Ernesto Lopez Torres,^{ab,q} Alice Manna,^{d,s} Michela Marafini,^{l,t} Maurizio Massa,^a Cristian Massimi,^{d,s} Ilaria Mattei,^h Alessio Mereghetti,^e Alberto Mengarelli,^d Andrea Moggi,^a Maria Cristina Montesi,^{j,r} Maria Cristina Morone,^{m,y} Matteo Morrocchi,^{a,b} Silvia Muraro,^h Alessandra Pastore,^{aa} Nadia Pastrone,^q Vincenzo Patera,^{l,u} Francesco Pennazio,^q Marco Pullia,^e Luciano Ramello,^{aj} Claire-Anne Reidel,^f Riccardo Ridolfi,^{d,s} Valeria Rosso,^{b,a} Claudio Sanelli,^g Alessio Sarti,^{l,u} Gabriella Sartorelli,^{d,s} Osamu Sato,ⁱ Simone Savazzi,^e Lorenzo Scavarda,^{ah} Angelo Schiavi,^{l,u} Christoph Schuy,^f Emanuele Scifoni,^o Adalberto Sciubba,^{g,u} Alexandre Sécher,ⁿ Marco Selvi,^d Mario Sitta,^{q,ai} Roberto Spighi,^d Eleuterio Spiriti,^g Giancarlo Sportelli,^{b,a} Achim Stahl,^c Sandro Tomassini,^g Francesco Tommasino,^{o,p} Marco Toppi,^{l,u} Giacomo Traini,^l Antonio Trigilio,^{l,x} Giacomo Ubaldi,^{d,s} Valeri Tioukov,^j Alessandro Valetti,^{q,z} Serena Marta Valle,^h Marie Vanstalle,ⁿ Mauro Villa,^{d,s} Ulrich Weber,^f Roberto Zarrella,^{d,s} and Antonio Zoccoli^{d,s}

*Corresponding author.

- ^a*Istituto Nazionale di Fisica Nucleare (INFN), Section of Pisa, Pisa, Italy*
- ^b*University of Pisa, Department of Physics, Pisa, Italy*
- ^c*RWTH Aachen University, Physics Institute III B, Aachen, Germany*
- ^d*Istituto Nazionale di Fisica Nucleare (INFN), Section of Bologna, Bologna, Italy*
- ^e*Centro Nazionale di Adroterapia Oncologica (CNAO), Pavia, Italy*
- ^f*Biophysics Department, GSI Helmholtzzentrum für Schwerionenforschung, Darmstadt, Germany*
- ^g*Istituto Nazionale di Fisica Nucleare (INFN), Laboratori Nazionali di Frascati, Frascati, Italy*
- ^h*Istituto Nazionale di Fisica Nucleare (INFN), Section of Milano, Milano, Italy*
- ⁱ*Nagoya University, Department of Physics, Nagoya, Japan*
- ^j*Istituto Nazionale di Fisica Nucleare (INFN), Section of Napoli, Napoli, Italy*
- ^k*Istituto Nazionale di Fisica Nucleare (INFN), Section of Perugia, Perugia, Italy*
- ^l*Istituto Nazionale di Fisica Nucleare (INFN), Section of Roma 1, Rome, Italy*
- ^m*University of Rome Tor Vergata, Department of Physics, Rome, Italy*
- ⁿ*Université de Strasbourg, CNRS, IPHC UMR 7871, F-67000 Strasbourg, France*
- ^o*Trento Institute for Fundamental Physics and Applications,
Istituto Nazionale di Fisica Nucleare (TIFPA-INFN), Trento, Italy*
- ^p*University of Trento, Department of Physics, Trento, Italy*
- ^q*Istituto Nazionale di Fisica Nucleare (INFN), Section of Torino, Torino, Italy*
- ^r*University of Napoli, Department of Physics “E. Pancini”, Napoli, Italy*
- ^s*University of Bologna, Department of Physics and Astronomy, Bologna, Italy*
- ^t*Museo Storico della Fisica e Centro Studi e Ricerche Enrico Fermi, Rome, Italy*
- ^u*University of Rome La Sapienza, Department of Scienze di Base e Applicate per l’Ingegneria (SBAI),
Rome, Italy*
- ^v*University of Perugia, Department of Physics and Geology, Perugia, Italy*
- ^w*University of Perugia, Department of Engineering, Perugia, Italy*
- ^x*University of Rome La Sapienza, Department of Physics, Rome, Italy*
- ^y*Istituto Nazionale di Fisica Nucleare (INFN), Section of Roma Tor Vergata, Rome, Italy*
- ^z*University of Torino, Department of Physics, Torino, Italy*
- ^{aa}*Istituto Nazionale di Fisica Nucleare (INFN), Section of Bari, Bari, Italy*
- ^{ab}*CEADEN, Centro de Aplicaciones Tecnológicas y Desarrollo Nuclear, Havana, Cuba*
- ^{ac}*Gran Sasso Science Institute, L’Aquila, Italy*
- ^{ad}*Technische Universität Darmstadt Institut für Festkörperphysik, Darmstadt, Germany*
- ^{ae}*National University of Science and Technology, MISIS, RUS-119049 Moscow, Russia*
- ^{af}*Lebedev Physical Institute of the Russian Academy of Sciences, RUS-119991 Moscow, Russia*
- ^{ag}*University of Bari, Department of Physics, Bari, Italy*
- ^{ah}*ALTEC, Aerospace Logistic Technology Engineering Company, Corso Marche 79, 10146 Torino, Italy*
- ^{ai}*Dipartimento di Scienze e Innovazione Tecnologica, Università del Piemonte Orientale,
Alessandria, Italy*
- ^{aj}*Dipartimento per lo Sviluppo Sostenibile e la Transizione Ecologica, Università del Piemonte Orientale,
Vercelli, Italy*

E-mail: leonello.servoli@pg.infn.it

ABSTRACT: The goals of the FOOT (FragmentatiOn Of Target) experiment are to measure the proton double differential fragmentation cross-section on H, C, O targets at beam energies of interest for hadrontherapy (50–250 MeV for protons and 50–400 MeV/u for carbon ions), and also at higher energy, up to 1 GeV/u for radioprotection in space. Given the short range of the fragments, an inverse kinematic approach has been chosen, requiring precise tracking capabilities for charged particles. One of the subsystems designed for the experiment will be the MSD (Microstrip Silicon Detector), consisting of three x-y measurement planes, each one made by two single sided silicon microstrip sensors. In this document, we will present a detailed description of the first MSD prototype assembly, developed by INFN Perugia group and the subsequent characterization of the detector performance. The prototype is a wide area ($\sim 100\text{ cm}^2$) single sensor, $150\text{ }\mu\text{m}$ thick to reduce material budget and fragmentation probability along the beam path, with $50\text{ }\mu\text{m}$ strip pitch and 2 floating strip readout approach. The pitch adapter to connect strips with the readout channels of the ASIC has been implemented directly on the silicon surface. Beside the interest for the FOOT experiment, the results in terms of cluster signal, signal-to-noise ratio, dynamic range of the readout chips, as well as long-term stability studies in terms of noise, are relevant also for other experiments where the use of thin sensors is crucial.

KEYWORDS: Particle tracking detectors; Particle tracking detectors (Solid-state detectors); Si microstrip and pad detectors; Solid state detectors

Contents

1	Introduction	1
2	Material and methods	3
2.1	Assembly procedure	5
2.2	DAQ system and data taking	6
2.3	Pedestal, common mode noise and single strip noise	7
2.4	Cluster finding algorithm	9
3	Results	10
3.1	Common mode noise variation	10
3.2	Single strip noise determination	11
3.3	Pedestal and noise stability in time	11
3.4	Characterization with charged particles	12
4	Discussion	14
5	Conclusions	15

1 Introduction

The treatment of solid tumors using charged particles, protons or heavier ions, called hadrontherapy, was proposed by Wilson [1], and it is gaining momentum in recent years [2] due to some desirable properties of these external beams, among which small multiple scattering, energy rate deposition along the path in the human body almost inversely proportional to distance traveled until the particles enters in the *Bragg peak* region, few millimeters wide, where most of the energy carried by the charged particle is released. These properties make it possible to irradiate intensely a strictly localized region within the body while sparing tissues before, after and near the target region.

The energy deposition rate due to electromagnetic ionization from heavy charged particles is very well known, allowing the Treatment Planning Systems to produce accurate irradiation plans. However the same is not true for the other components of energy loss for heavy charged particle in matter, namely the nuclear fragmentation of both projectile (for ions) and target along the path to the tumor region. Secondary particles produced by beam and target fragmentation have very high Linear Energy Transfer and, therefore, high Relative Biological Effectiveness (RBE) and contribute to the total dose released, especially in healthy tissues on the path to the tumor region. Since these fragments produced by the interaction of protons with the target nuclei have a short range (e.g. order of 10 to 100 μm) in the 50–200 MeV/nucleon energy range, it is very challenging to detect them and to obtain the relative cross sections. The FOOT experiment [3] aims to fill these experimental gaps using the inverse kinematics technique to identify fragments and measure their energy. The

cross sections will be obtained subtracting the ones of ions on a target rich in protons, like C_2H_4 , from the ones of ions on pure C target, like graphite. The experimental apparatus used for this task has been designed to be as compact as possible to be easily transported to centres equipped with structures capable of accelerating the ion beams to the required energy. The experiment foresees two different configurations: one with electronic detectors to precisely measure heavier fragments ($Z \geq 3$) and some capability for lighter ions, and one mainly based on emulsion chambers for the precise measurement of the lighter fragments ($Z \geq 1$).

Different regions can be identified for the electronic configuration (figure 1):

Interaction region: a 250 μm thick plastic scintillator, used to provide trigger information and start time to the Time Of Flight (TOF) detector, a drift chamber [4] to measure the direction of the beam and thin polyethylene and graphite targets.

Tracking system: a vertex detector consisting of four layers of silicon pixel sensors after the target, two permanent magnets with Halbach geometry with two layers of silicon pixel detectors in the centre and finally three planes of microstrip detectors (MSD), each consisting of 2 mutually orthogonal single-sided sensors 150 μm thick, with position from the target in the range 25–40 cm, to be optimized according to the specific beam type and energy, to reconstruct the x-y position and to perform the momenta measurement.

Time-of-Flight and Calorimetric region: the TOF Wall is built by 20 + 20 plastic scintillator bars arranged in two orthogonal layers to measure the deposited energy ΔE , provides the STOP signal for the TOF measurement and an estimate of the fragment position [5].

The calorimeter consists of ~ 320 BGO crystal elements (exact number will depend on the final calorimeter configuration), each read out by a 25 SiPM matrix. It is the last detector along the beam line and its task is to measure the kinetic energy of fragments [6].

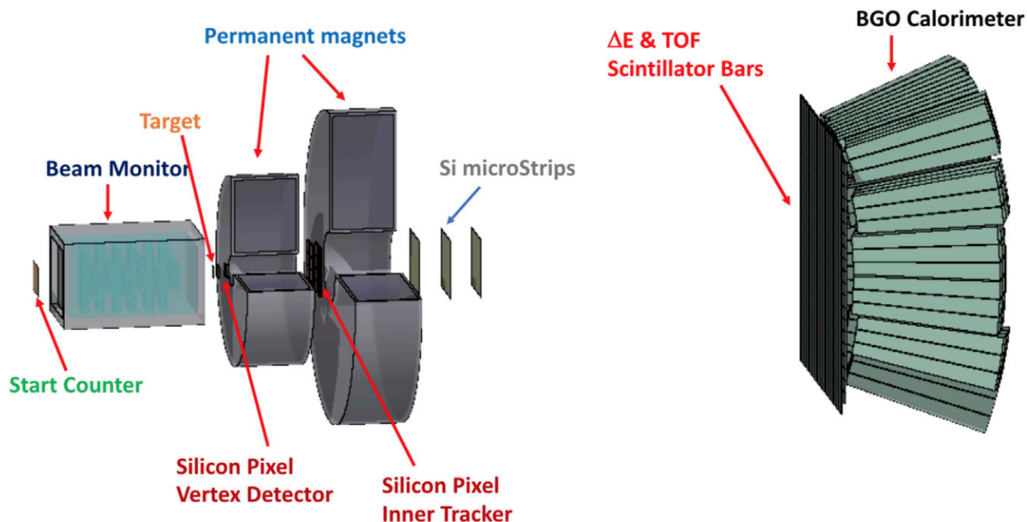


Figure 1. The FOOT Experiment with its components.

The second configuration, based on an emulsion chamber that will replace the electronic setup and act as target after the interaction region, will supply measurements for lighter fragments emitted at larger angles, extending the angular acceptance up to about 70° [7].

This paper reports the characterization of the first silicon microstrip sensor prototype of the MSD. The performances in terms of signal, signal-to-noise ratio and dynamic range of the reading chips for charged particles and long-term stability in terms of noise have been studied.

2 Material and methods

The MSD apparatus is the last tracking station of the magnetic spectrometer and beside the spatial position resolution and the energy deposition measurements, will satisfy the request for geometric acceptance at $\pm 10^\circ$ with a wide area sensor, $10 \times 10 \text{ cm}^2$. To avoid the need of further material along the beam path, a front-to-front configuration has been adopted, the sensor's metalized backplanes facing the outside to shield the silicon from ambient light. Furthermore this solution is flexible allowing to vary the number of planes simply adding independent units along the beam line.

Two AC-coupled silicon microstrip sensor, each read-out by ten IDE1140 ASIC chips [8] and mutually orthogonal will be the components of each MSD x-y plane. The material crossed by the charged particle must be thick enough to create a sufficiently large number of electron-hole pairs without introducing an excessive deviation due to multiple scattering from the original trajectory or increasing the probability of nuclear fragmentation. For MSD case, the sensors chosen, made by Hamamatsu Photonics, are only $150 \mu\text{m}$ thick, half the standard thickness for tracking sensors. The expected MIP signal will be high enough to be detected with good efficiency ($\text{SNR} \sim 6\text{--}7$ [9]), and the ions will give an even higher signal. The sensor has a $96 \text{ mm} \times 96 \text{ mm}$ active area segmented in 1920 strips with a $50 \mu\text{m}$ implantation pitch (figure 2a-b). A further innovation in these sensors to help the assembly procedure is the pitch adapter directly designed on the silicon (figure 2b) to reduce the bonding procedure complexities.

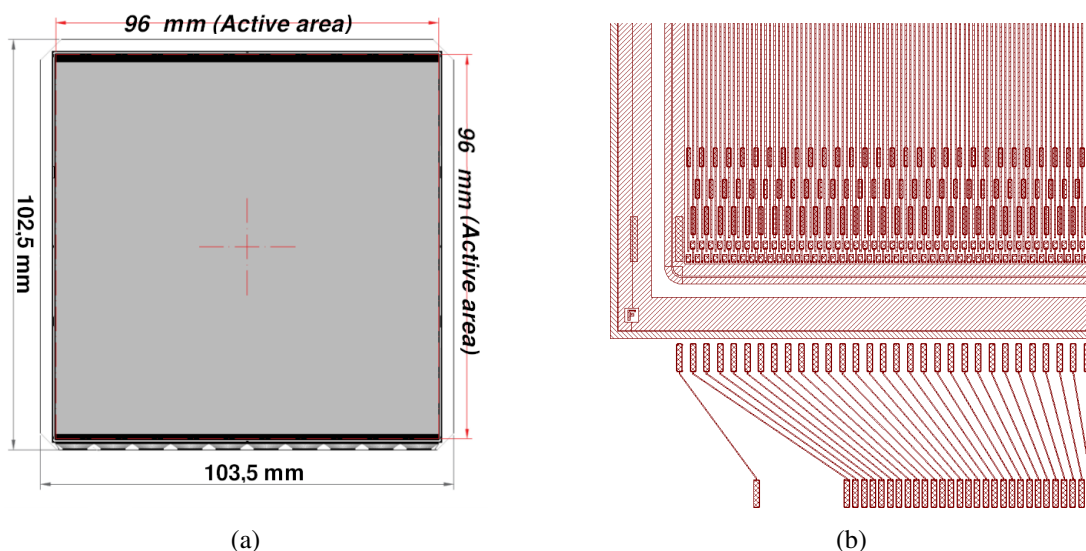


Figure 2. Technical drawings of (a) the silicon sensor and (b) the on-silicon pitch adapter.

A charged particle passing through the silicon sensor will deposit energy along the track creating e-h pairs (figure 3); the charge carriers drift toward the electrodes to be collected. The deposited energy depends on the particle type and energy, and a value of ≈ 24000 e-h pairs for $300\ \mu\text{m}$ track length is used for Minimum Ionizing Particles. For $150\ \mu\text{m}$ thick sensor, the value is reduced to ~ 11800 e-h [10]. An external electric potential to deplete the entire thickness of the sensor assures the collection of the produced charges. For $150\ \mu\text{m}$ thick sensor the complete depletion should be reached at ~ 20 V, which is compatible with the value provided by the vendor for the sensor used to build the first prototype (FOOT_PE1). The bias voltage chosen for all the tests was set at 50 V to work in the *over depletion* regime to assure a complete charge collection efficiency and thus obtain the highest possible signal.

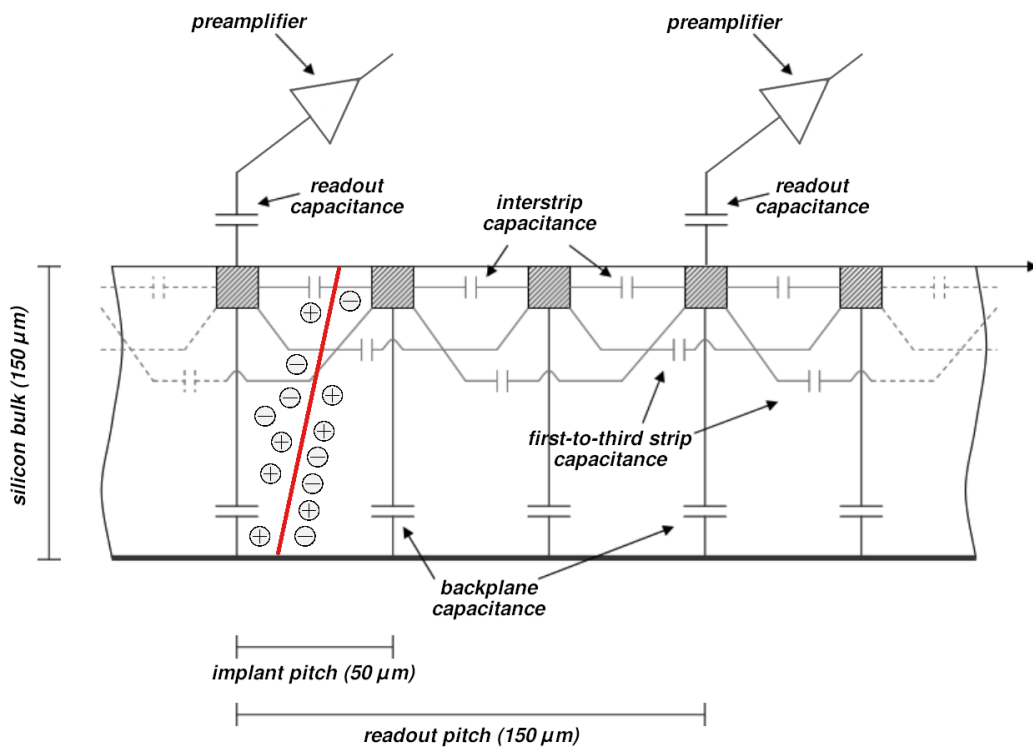


Figure 3. Sensor section with electric scheme and incident charged particle.

The charge distribution via the capacitive coupling of the readout strips allows for a spatial resolution on the order of $10\ \mu\text{m}$ or even less for a strip pitch of $50\ \mu\text{m}$ [11]. The spatial resolution requested for MSD is $\sim 40\ \mu\text{m}$. To optimize the costs of the readout chips maintaining the spatial resolution below the requirements, a readout pitch of $150\ \mu\text{m}$, with two unconnected strips (floating strips) between two readout strips has been chosen given its digital spatial resolution of $43\ \mu\text{m}$. With the analog readout at least a gain of a factor 2 for spatial resolution is expected with this implementation from past experiences [12, 13]. Table 1 summarizes the main characteristics of MSD sensors.

Table 1. Silicon sensor specifications from Hamamatsu.

Thickness	150 μm
Overall dimensions	102.5 mm \times 103.5 mm
Active area	96 mm \times 96 mm
Total nr of strips	1920
Readout strips in FOOT	640
Readout pitch	150 μm
Implant pitch	50 μm
Mechanical edges	5 mm
Bonding pad dimensions	80 \times 300 μm^2
Strip width	40 μm

2.1 Assembly procedure

The construction of the first FOOT MSD sensor prototype was used to develop the assembly procedure and check for the basic electrical performances with and without ionizing radiation. The prototype was assembled combining established methodologies with some innovative choices and instruments. The basic procedure can be described as follows:

- electrical testing of the hybrid board;
- gluing and micro-bonding of the IDE1140 chips: the custom hybrid board already contains all the passive circuitry needed, and only the readout ASICs need to be glued and micro-bonded;
- precise alignment of the hybrid on the assembly jig to ensure the correct positioning of all the components to $\sim 100 \mu\text{m}$ uncertainty;
- positioning of the silicon sensor on the hybrid: the pins used to align the hybrid board to the jig are designed in a D-like shape so that once the sensor is correctly aligned the flat side of the pins can be used to remove the pins without damaging the sensor; it should be underlined that given the reduced thickness, specific tools to handle the sensor, like the 4-pod vacuum suction shown in figure 4(left), were designed and realized; at the same time to assure the uniform pressure needed during the glue of the sensor on hybrid, another specific tool has been designed and used, figure 4(center and right), with a weight over it;
- after curing of the glue, in order to check the alignment and measure the thickness of the detector, the metrology measurement is done and then the wire bonding is performed;
- after assembly, the completed sensor is then electrically tested to check its quality.

Figure 5 shows the prototype sensor (FOOT_PE1) after the completion of the assembly procedure. The *IDE1140-Silicon* bond is the only one needed with the use of the pitch adapter directly designed on the silicon sensor.

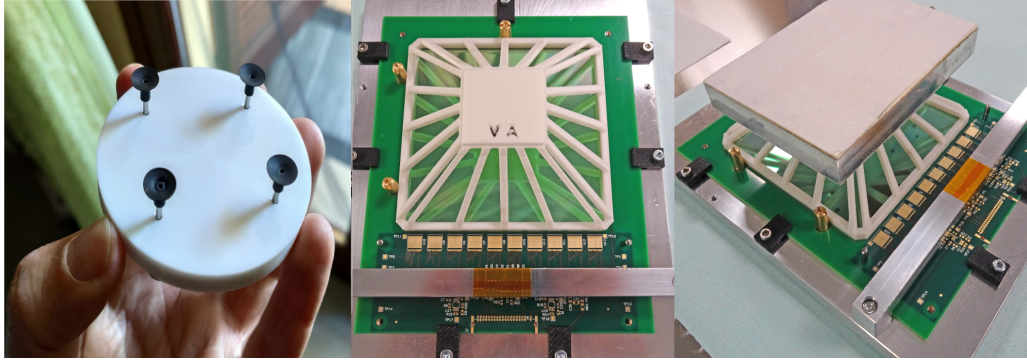


Figure 4. Custom tools for assembly: pickup tool with 4 suction cups (left); tool to distribute pressure for sensor gluing on hybrid board (center and right pictures).

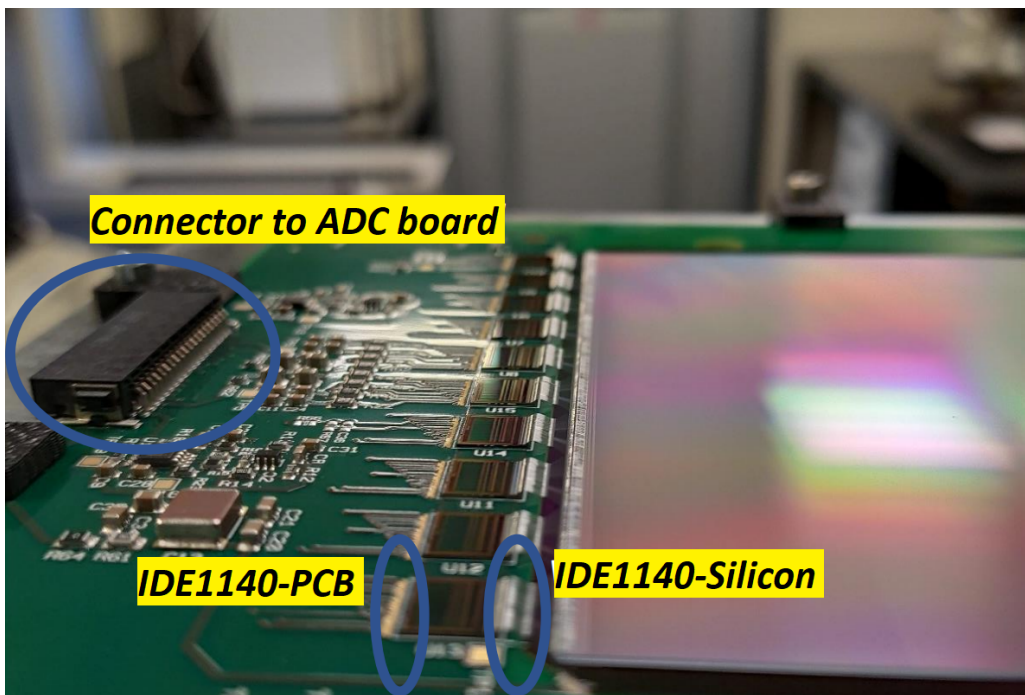


Figure 5. Closeup of FOOT_PE1 after IDE1140 and sensor bonding. The two array of bonds between respectively silicon strips and ASIC channels and ASIC chip and hybrid board are circled in blue. Also the connector to the ADC board is circled on the left.

2.2 DAQ system and data taking

The front-end hybrid board collects and amplifies the signals coming from the strips with the use of 10 IDE1140 ASICs (10×64 channels low-noise/ low power high dynamic range preamplifier-shaper circuit) produced by IDEAs. The IDE1140 chips are organized into two independent readout groups: the two groups are read in parallel while the chips of each group are serially readout. Each group has its amplification circuit, whose analogical output is then transferred to the DAMPE miniTRB data acquisition board [14] containing 2 ADCs and an FPGA. The board has the task of digitizing the data from the IDE1140 chips, packing them in binary format and sending them to the DAQ program

running on the control PC to store them on a hard disk for further offline processing. The miniTRB can also generate an internal random trigger at 50 Hz or receive an external trigger signal.

A plastic scintillator bar read by a phototube is placed under the sensor to trigger when an ionizing charged particle coming from the other side passes through the sensor. The entire setup is enclosed in a shielding box to protect from light and electromagnetic noise from laboratory sources.

According to measurements from Hamamatsu, the depletion voltage of the sensor is around 20 V, so in the following work, we have chosen to work with 50 V bias to overdeplete the sensor for complete charge collection. The first operational tests were carried out to assess the correct electrical behaviour of the digital part of the readout hybrid, the reconstruction of the raw event and the compatibility of the acquired signals with the expected values for the readout ASIC.

2.3 Pedestal, common mode noise and single strip noise

Before searching for charged particle signals, it is of fundamental importance to characterize the noise of the assembled detector. One event is the raw content of all the prototype strips, i.e. 640 integer values grouped in 10 blocks with a range from 0 to 4095 ADCs. A set of consecutive events is a run. A calibration run is a collection of a minimum of 3000 up to 10000 events, without external radiation source, to calibrate the sensor's response. Figure 6 shows one event: all channels have a value between 150 and 300 ADCs determined both by the ADC offset (settable via a potenziometer on the miniTRB board), the difference among the readout channels of the IDE1140 chips and the sensor characteristics.

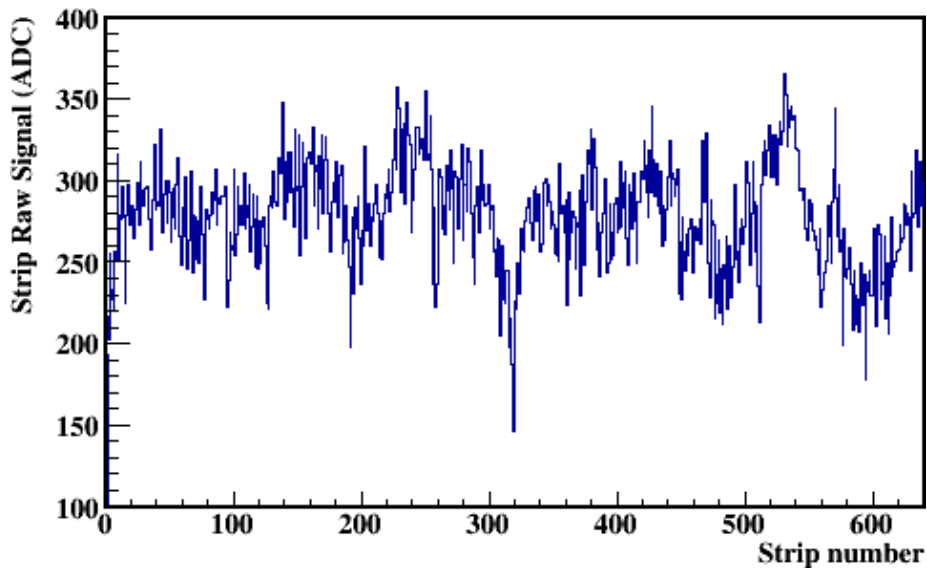


Figure 6. Sample raw event display for a pedestal run.

As an example, figure 7(left) shows the raw output in ADC of strip # 600 during a calibration run. The average response of the single strips in the absence of an external radiation source should be determined and then subtracted to equalize the single strip response. The average is the pedestal of a channel and is defined as

$$\text{ped}_i = \frac{1}{N} \sum_j^N (\text{ADC}_{ij}) \quad (2.1)$$

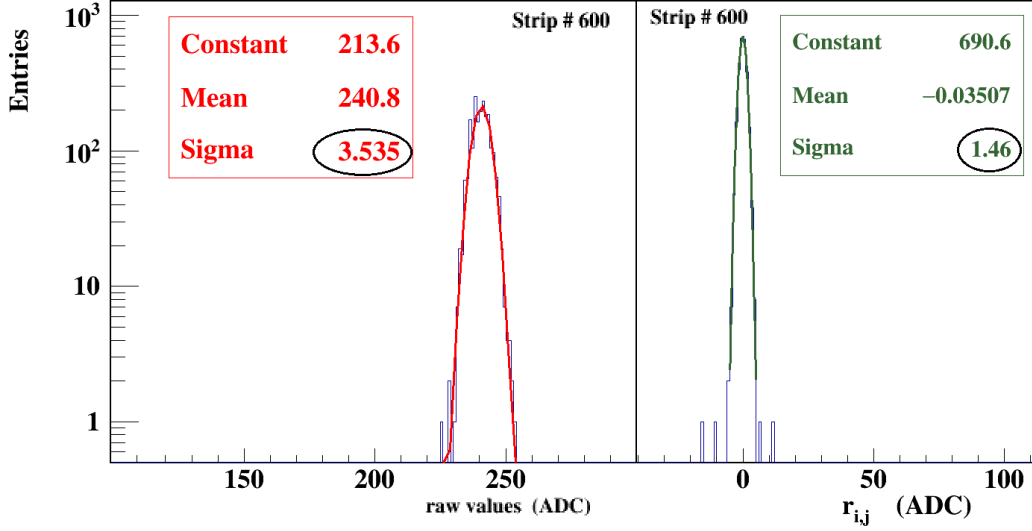


Figure 7. Strip # 600: distribution of raw output values (left) and after pedestal and common mode subtraction (right).

where ped_i is the pedestal of channel i , j is the event number, N is the number of events used to compute the pedestal, ADC_{ij} is the raw signal of strip i for event j .

For strip # 600, the pedestal is 241 ADC while the fluctuation of the channel content in dark conditions is ~ 3.5 ADC. The distribution of all the pedestals of the PE001 prototype is a gaussian whose mean value is 277 ADC and its width is 31 ADC, i.e. roughly double of the estimated signal range for a MIP (~ 15 ADC) found extrapolating the measure done using the same readout board with a $300 \mu\text{m}$ thick sensor and scaling it down via SRIM simulation to a $150 \mu\text{m}$ sensor [9]. Hence the equalization of strip by strip response is mandatory to properly analyze the presence of a signal produced by a charged particle in a frame.

However because the pickup of external electromagnetic noise could produce a collective signal variation event by event, also this contribution should be subtracted from the raw strip values. The *common mode noise* (CN) is the average deviation, event by event, from their pedestals of all the channels read by a single ASIC [15, 16]. Hence *common mode noise* of event j (CN_j) is calculated as:

$$CN_j = \frac{1}{N_j} \sum_i^{N_j} (ADC_{ij} - ped_i) \quad (2.2)$$

where N_j is the number of good strips within the ASIC (noisy or dead strips are excluded).

The last operation, after pedestal and common mode fluctuations subtraction is the computation of *single strip noise* (σ_i). This information will be crucial to define a uniform criteria (strip signal higher than threshold) to evaluate if a signal is due to a noise fluctuation or not. The final reduced signal value for each channel is thus:

$$r_{ij} = ADC_{ij} - ped_i - CN_j \quad (2.3)$$

This formulation will be used in the signal finding algorithm in section 3.4.

Figure 7(right) shows the r_{ij} distribution for the strip # 600. Comparing with the raw value distribution on the right, the mean is translated at 0 ADC, and the width is now reduced to about half the previous value, implying that the uncertainty is reduced by the *common mode noise* subtraction.

Finally writing all the contributions to the r_{ij} uncertainty (σ_i) due to each of the terms of eq. (2.3) we obtain the following equation:

$$\sigma_i^2 = \sigma_{i,\text{intrinsic}}^2 + \sigma_{\text{CN}_j}^2 + \sigma_{i,\text{pedestal}}^2 \quad (2.4)$$

$\sigma_{i,\text{intrinsic}}$ is the response fluctuation of single strip due to the intrinsic characteristics of that strip and is the lower limit to the measurement precision.

σ_{CN_j} is the precision of the CN_j evaluation using chip j .

$\sigma_{i,\text{pedestal}}$ is the precision of the ped_i evaluation for strip i .

2.4 Cluster finding algorithm

If the track passes in the region between two strips (even if unconnected), the charge collection and signal formation are split in a non trivial way and readout by the two closest connected strips. Hence an algorithm to find the reconstruct the signal even if split among several adjacent strips is needed, and it should produce as observable a *cluster*.

The r_{ij} variable allows checking if a signal is over the noise level. The cluster finding algorithm parses the reduced values for one event and seeks the cluster seed (figure 8). A cluster seed is defined as a channel with the reduced value $r_{ij} > T_s$, where T_s is the seed threshold. When a cluster seed is found, neighboring channels are checked for values over the neighbour threshold T_f , until $r_{ij} < T_f$.

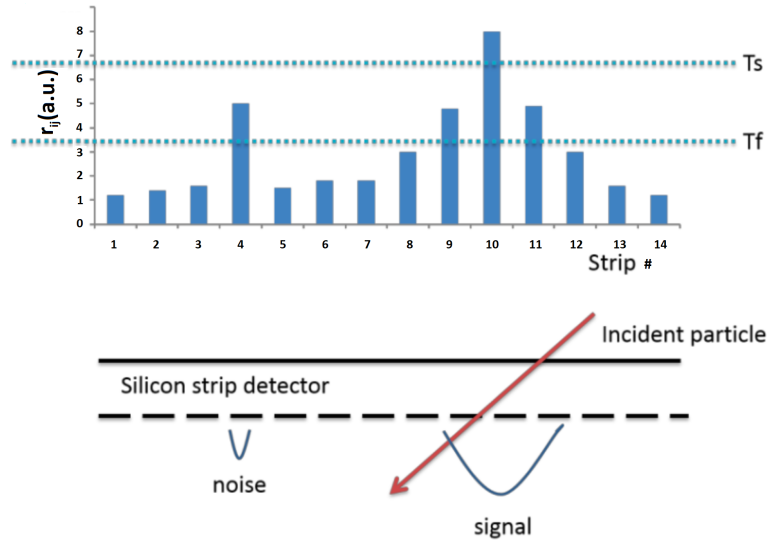


Figure 8. Scheme of the asymmetric clustering algorithm, with two thresholds T_s and T_f .

The properties of a cluster to be determined are:

- cluster position, i.e. the presumed position of the incoming charged particle;
- cluster charge, i.e. the sum of the strip signal for the strips belonging to the cluster;
- cluster width, i.e. the number of strips belonging to the cluster.

In a floating strip configuration, the induced current by an unconnected strip will be shared with losses with respect to the connected ones [12]. This signal subdivision is dependent in a non-trivial way on the track's position with respect to the electrodes, the number of floating strips and their characteristics. A reduction of up to 50% of the full signal is possible and could be corrected only with the knowledge of the η function [17]. In this study, we do not have an external evaluation of the track position, hence the results will be the average response of tracks crossing the sensor with an uniform spatial distribution, without cluster signal correction for the impact position.

3 Results

After completion of the detector's assembly, its behaviour has been thoroughly verified both without and with particle sources following the procedure outlined in section 2.3.

3.1 Common mode noise variation

Figure 9 shows the distribution of the CN for all the events collected during one calibration run. The distribution is correctly fitted by a Gaussian whose $\sigma \sim 3$ ADC counts corresponds to ~ 20 – 25% of a MIP. This implies that the event-by-event subtraction of *common mode noise* is necessary to correctly evaluate the signal, especially for MIP particles.

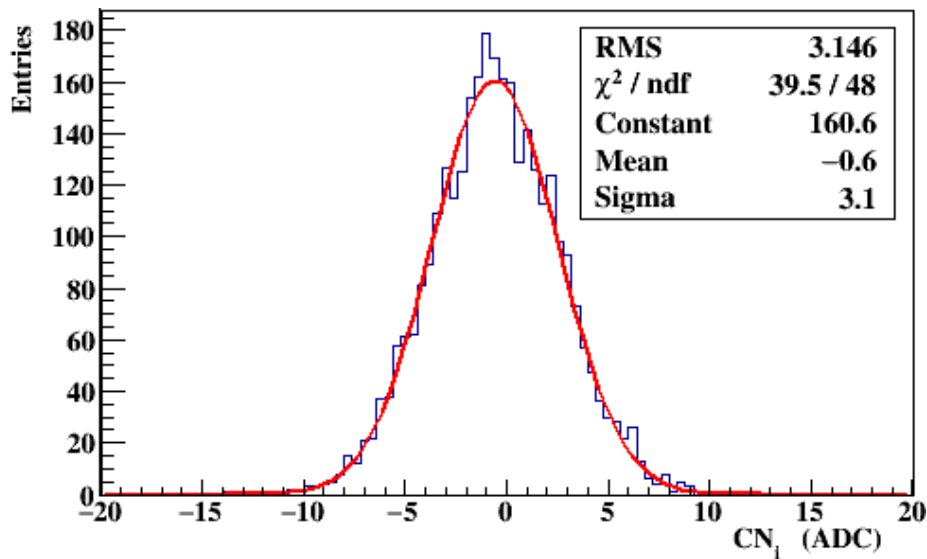


Figure 9. Common mode noise distribution for one chip for a calibration run.

In principle, the *common mode noise* could change for each of the electronic units that pick up the external noise. In the FOOT_PE1 case, this could be both a single front-end unit, the IDE1140 chip, or one of the ADC circuits. If one or more chips have so many strips with signal such that CN_j could not be computed, the CN_j value from other chips could be used. Hence the study of the CN_j uniformity across the whole sensor is an important task.

The distribution of the event-by-event difference of one IDE1140 chip with respect to the average value of the other four chips read by the same ADC is a Gaussian distribution with mean 0.0 ± 0.4 ADC, so there is no substantial difference in using one chip or another.

Finally the distribution of the difference of the common mode computed by the two different ADC chains is a Gaussian with mean 0.0 ± 0.6 ADC confirming thus the possibility to use other chips to compute the *Common Mode* correction event by event.

3.2 Single strip noise determination

Applying eq. (2.3) and computing σ_i we obtain the profile along the sensor shown in figure 10 with an average value $\overline{\sigma}_i$ of 1.54 ± 0.12 ADC. From this value and the average pedestal value, the dynamic range available is ~ 2430 times the $\overline{\sigma}_i$.

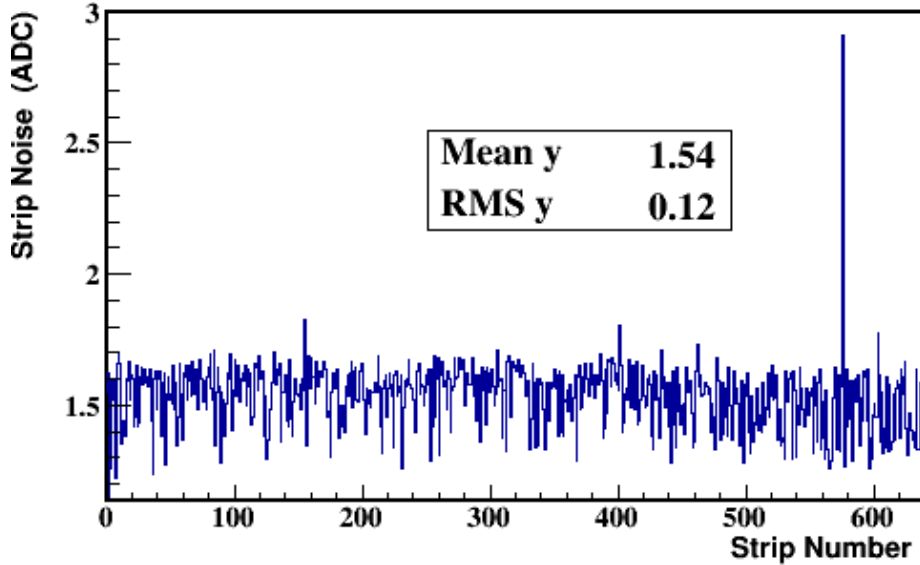


Figure 10. Strip noise profile for all FOOT_PE1 strips.

In order to evaluate instead the $\sigma_{i,\text{intrinsic}}$ value we have to apply eq. (2.4), so we obtained the single terms:

The average value of $\overline{\sigma_{i,\text{pedestal}}}$ is about 0.079 ± 0.003 ADC; hence this contribution being smaller than the others will be negligible in the computation of the single strip noise.

Chip # 5, where strip # 600 studied on 7 is connected, has an average uncertainty on CN_5 of 0.23 ± 0.03 ADC. All the other chips have σ_{CN_j} values close to the one of chip # 5, for an average over all chips of 0.25 ± 0.05 ADC.

Subtracting σ_{CN_j} contribution and considering negligible the value of $\sigma_{i,\text{pedestal}}$, the average $\overline{\sigma_{i,\text{intrinsic}}}$ for the FOOT_PE1 prototype is 1.52 ADC, leading to a dynamic range of $2450 \overline{\sigma_{i,\text{intrinsic}}}$.

Because this value is compatible with average $\overline{\sigma}_i$, and the dynamic range is also substantially the same, we will use the latter one, easier to implement, to define the threshold to select in a frame strips with signal from the ones without.

3.3 Pedestal and noise stability in time

The stability of pedestals, common noise and single strip noise were studied over several hours of the detector's operation, keeping the same operational settings, to understand the needed calibration frequency to ensure a correct signal extraction.

A run where no signal source is present was used to analyze short-term stability, with the DAQ system running for several hours using the internal 50 Hz periodic trigger. To check the time variation of pedestal and CN_j , corresponding values are first plotted as function of the acquisition time for each strip. Common Noise is expected to be quite stable since the tests are performed in a controlled lab environment with no external sources of noise like magnetic fields or other detectors working. Figure 11 reports the variation with time of the pedestal of a typical strip averaged over 2 minutes intervals. The stability is assessed numerically fitting the data with a polynomial of degree one. The slope has a value compatible with 0 demonstrating substantial stability of the pedestal over 3 hours. The distribution of slopes for all strips is well represented by a Gaussian with mean value 0.000 ± 0.001 ADC/minutes.

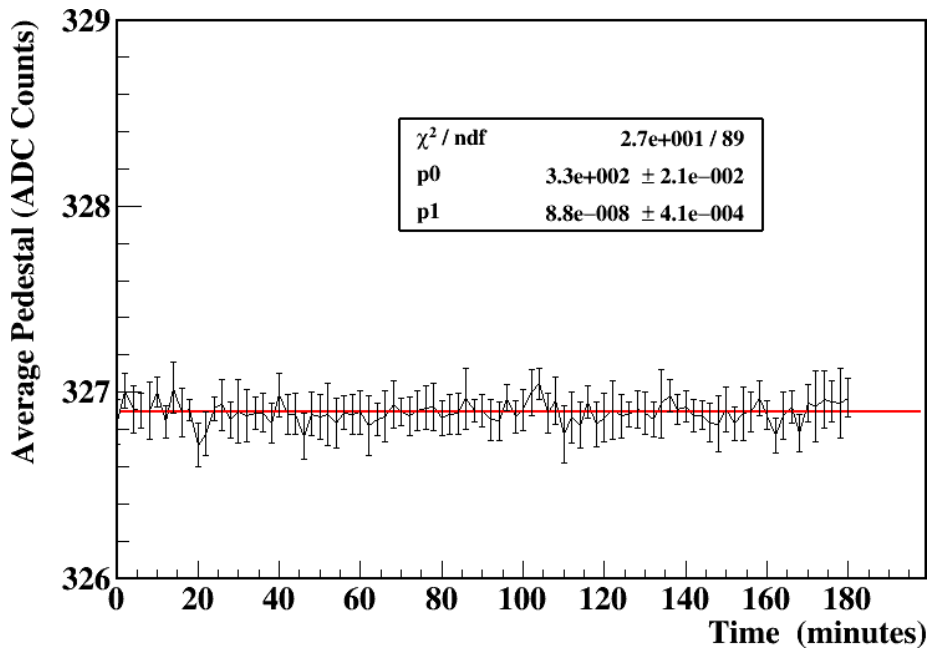


Figure 11. Single strip pedestal value variation over time. Each point is averaged over 2 minutes interval.

3.4 Characterization with charged particles

We have used cosmic rays to test the sensor prototype, hence we have used the *Weightfield2* software package [18] to simulate the interaction of a MIP particle in a p over n sensor. The aim is to understand the expected lateral diffusion of the signal produced by a MIP crossing a 25 V depletion voltage detector reverse biased at 50 V (same as the FOOT_PE1). Figure 12 shows the spatial charge distribution for the electrons generated by the ionization of the particle crossing the bulk under one of the readout strips: the lateral distribution is of the order of a few micrometers even taking into account the thermal distribution. Due to the intense electric field, the charge will be collected solely on that strip. If the track passes in the region between two strips (even if unconnected), the charge collection and signal formation are split on the two strips. Hence an algorithm to find the complete signal even if split among several adjacent strips is needed, and it should produce as observable a *cluster*.

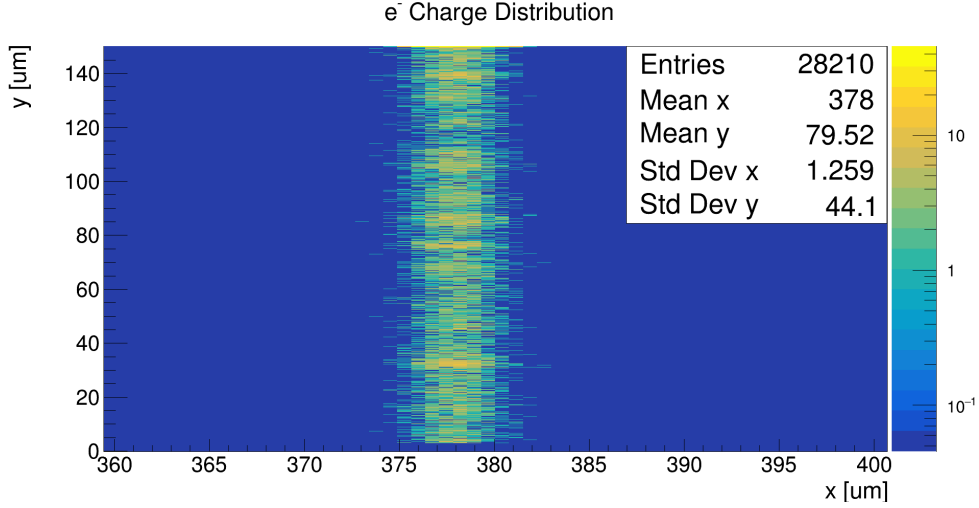


Figure 12. Charge distribution in the detector bulk for the ionization electrons.

To define the proper T_s threshold to be used, we have to reduce the probability for one strip to be over the threshold in one frame. Figure 13 shows the cumulative distribution of the strips with r_{ij} over threshold normalized to the single strip noise σ_i as a function of the threshold. At threshold = 4 the probability to have one strip in the event over the threshold due to noise fluctuations is $\sim 5\%$.

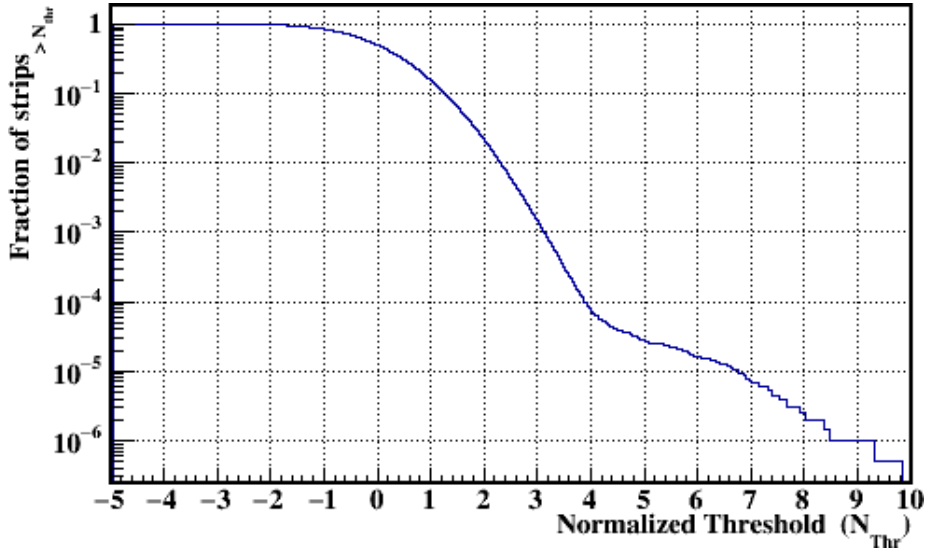


Figure 13. Integral distribution of strips with signal r_{ij} higher than seed threshold T_s vs seed threshold. Seed threshold is normalized to σ_i of each strip.

Hence fixing $T_s = 4$ and $T_f = 2$ to reconstruct the cluster, and selecting only frames with just one cluster, the distribution of cluster signals is shown in figure 14. Signal distribution is fitted with a convolution of a Gaussian function with a Landau function to account for the energy loss in the sensor and the noise in the sensor and electronics [16, 19]. The fit results in a Most Probable Value (MPV) of $\approx 17.5 \pm 0.2$ ADC, a value that is close to the predicted value obtained in [9]. The Cluster Signal/ σ_{ij} is ~ 10 , a value sufficient for MIP identification with $\sim 95\%$ efficiency (see Discussion section).

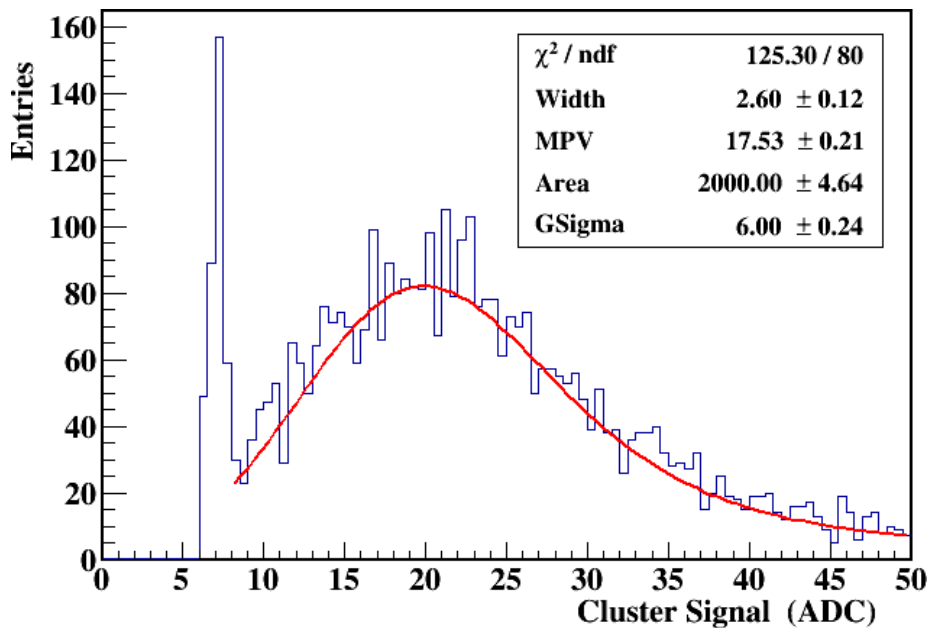


Figure 14. Cluster signal distribution for cosmic muons data.

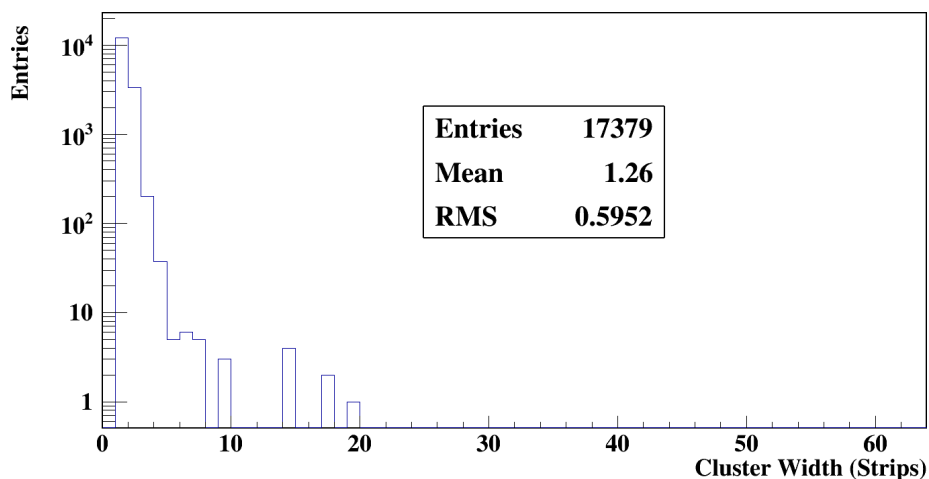


Figure 15. Cluster width distribution for cosmic muons data.

Finally, figure 15 shows the cluster width distribution and the average value ~ 1.3 strip. The few events at higher cluster width are due to cosmic rays intersecting the scintillator bar used for the trigger at an angle that would correspond to a grazing angle [20] in the silicon so that many strips would be interested by the energy deposition of the event.

4 Discussion

The assembly procedure and the dedicated ad-hoc tools worked perfectly assuring a smooth production procedure for the prototype. The fabrication of the pitch adapter directly on the silicon simplified the bonding procedure and produced no bad channels in the readout.

The *common mode noise* event-by-event computation does not depend from the readout ASIC or the ADC chain, hence if a block of 64 channels could not be used in one event, it is possible to use the other blocks to compute the *common mode noise* correction without introducing a relevant uncertainty.

The *single strip noise* has been measured and is at the level of 1.5 ADC, close to the minimum value of 0.8 ADC, leading to an approximate dynamic range of $2430 \overline{\sigma}_i$. σ_i has been chosen as the reference strip parameter to be used in the signal searching by the clustering algorithm.

The result obtained in section 3.3 let us conclude that the single strip pedestals are stable at about the level of σ_i (2–3 ADC units) over ~ 10 hours for $\sim 99\%$ of the strips, at least in the laboratory environment. Hence during data taking, it should be safe to assume that a calibration taken at a certain point in time would be valid for few hours. However, this must be checked against common mode noise when going in an external data-taking campaign.

The Cluster Signal for a MIP has a MPV about 10 times the single strip noise σ_{ij} . This implies the capability to detect a MIP with $> 95\%$ efficiency as can be inferred from figure 14, evaluating the region below the fit for Cluster Signal < 8 ADC with respect to the total region under the fit function. Concerning the fake clusters, an estimation could be extracted by figure 13. The threshold at 4 implies that because of single strip noise of $8 \cdot 10^5$, for each event we have $\sim 5\%$ probability to have a strip over the threshold. This is confirmed by the peak at lower signal on cluster signal distribution, that has an area of $\sim 6\%$ of the entire distribution.

The cluster width equal to 1.3 is compatible with the expectation of a microstrip sensor with $50 \mu\text{m}$ space between two floating strips, meaning 2 strip clusters, and $100 \mu\text{m}$ between a readout strip and a floating strip, where we have most likely a single strip signal. Because of the uniform distribution of cosmic muon impact points on the sensor surface, we have 1/3 of events with 2 strip clusters and 2/3 with 1 strip clusters, that give an average of 1.3 strip per cluster.

The MPV for a MIP, the average pedestal value and the 12 bit ADC let us infer that the detector and its readout chain are capable in principle to read a signal of 210–220 MIPs on each strip. In the FOOT experiment, considering that the maximum Z will be 8, a factor 64 in energy deposition should be considered. Finally, also the $\beta < 1$ regime of fragments should be considered. For example for 200 MeV/u a total multiplicative factor of 197 should be taken into account, still below the measured dynamic range of 210–220 MIPs. Furthermore, even for fragments with lower energy, say 100 MeV/u, considering the splitting of the signal among two adjacent strips, the MSD dynamic range should be enough to collect the signal maintaining its linearity with deposited energy.

These results confirm that the first sensor prototype built for the MSD tracking system of the FOOT experiment satisfies the required characteristics. Also we have demonstrated that it is possible to build a thin wide area single sided silicon microstrip sensor maintaining good performances on MIP detection, hence even much better for non MIPs like ions, reducing the material budget along the beam line.

5 Conclusions

We have built the first prototype single side microstrip sensor for the MSD tracking system of the FOOT experiment. Some innovative features were introduced: $150 \mu\text{m}$ sensor thickness, pitch adapter directly patterned on the sensor, use of the metallized backplane of the sensor to screen from

visible light. Optimized tools to handle the thin sensor properly have been developed to ensure the planarity of the device.

The device has been electrically tested, and the response in dark condition have been extracted: low common mode noise values, low single strip noise, ~ 1.5 ADC, uniform behaviour across the sensor. The pedestal and noise short and medium-term stability have been found to be sufficient for several hours of data taking.

A standard two-threshold cluster algorithm has been implemented and the cosmic muon signal has been reconstructed, with MPV values compatible with the expected ones from previous measurements with thicker sensors and an S/N ~ 10 for MIP particles.

We have demonstrated that it is possible to build a thin wide area single sided silicon microstrip sensor maintaining good performances on MIP detection, hence even much better for non MIPs like ions, reducing the material budget along the beam line. Future tests on beam lines will be devoted to the studying the response to protons and heavier ions and to the spatial resolution determination.

Acknowledgments

The FOOT Collaboration acknowledges the INFN for its support in building the MSD system. The authors affiliated to the INFN Section of Perugia contributed to the experimental work and the data analysis. All authors reviewed and approved the manuscript.

References

- [1] R.R. Wilson, *Radiological use of fast protons*, *Radiology* **47** (1946) 487.
- [2] M. Durante and H. Paganetti, *Nuclear physics in particle therapy: A review*, *Rept. Prog. Phys.* **79** (2016) 096702.
- [3] FOOT collaboration, *Measuring the impact of nuclear interaction in particle therapy and in radio protection in space: the FOOT experiment*, *Front. Phys.* **8** (2021) 1.
- [4] Y. Dong et al., *The Drift Chamber detector of the FOOT experiment: Performance analysis and external calibration*, *Nucl. Instrum. Meth. A* **986** (2021) 164756.
- [5] M. Morrocchi et al., *Performance Evaluation of the TOF-Wall Detector of the FOOT Experiment*, *IEEE Trans. Nucl. Sci.* **68** (2021) 1161.
- [6] L. Scavarda, *Design and performance of the calorimeter for the foot experiment*, *Nuovo Cim. C* **04-05** (2020) 123.
- [7] FOOT collaboration, *Charge identification of fragments with the emulsion spectrometer of the foot experiment*, *Open Phys.* **19** (2021) 383.
- [8] IDEAS, <https://ideas.no/> (2021).
- [9] FOOT collaboration, *Evaluation of double-sided silicon microstrip sensor for the FOOT experiment*, *Nucl. Instrum. Meth. A* **936** (2018) 36.
- [10] S. Meroli, D. Passeri and L. Servoli, *Energy loss measurement for charged particles in very thin silicon layers*, 2011 *JINST* **6** P06013.
- [11] J. Alcaraz et al., *The alpha magnetic spectrometer silicon tracker: Performance results with protons and helium nuclei*, *Nucl. Instrum. Meth. A* **593** (2008) 376 [Erratum *ibid.* **597** (2008) 270] [Erratum *ibid.* **503** (2009) 545].

- [12] D. Lietti, A. Berra, M. Prest and E. Vallazza, *A microstrip silicon telescope for high performance particle tracking*, *Nucl. Instrum. Meth. A* **729** (2013) 527.
- [13] PAMELA TRACKER collaboration, *Spatial resolution of double-sided silicon microstrip detectors for the PAMELA apparatus*, *Nucl. Instrum. Meth. A* **556** (2006) 100 [[hep-ex/0510012](#)].
- [14] F. Zhang et al., *A prototype silicon detector system for space cosmic-ray charge measurement*, *Chin. Phys. C* **38** (2014) 066101.
- [15] W. Kucewicz and M. Pilch, *Low noise silicon microstrip detector*, *Nucl. Phys. B Proc. Suppl.* **61** (1998) 330.
- [16] N. Manthos, G. Sidiropoulos and P. Vichoudis, *An efficient hardware design for rejecting common mode in a group of adjacent channels of silicon microstrip sensors used in high energy physics experiments*, *IEEE Nucl. Sci.* **53** (2006) 1045.
- [17] R. Turchetta, *Spatial resolution of silicon microstrip detectors*, *Nucl. Instrum. Meth. A* **335** (1993) 44.
- [18] F.e.a. Cenna, *Weightfield2: A fast simulator for silicon and diamond solid state detector*, *Nucl. Instrum. Meth. A* **796** (2015) 149.
- [19] K.S. Kolbig and B. Schorr, *A Program Package for the Landau Distribution*, *Comput. Phys. Commun.* **31** (1984) 97 [*Erratum ibid.* **178** (2008) 972].
- [20] S. Meroli, D. Passeri and L. Servoli, *Measurement of charge collection efficiency profiles of CMOS active pixel sensors*, *2012 JINST* **7** P09011.